Author(s): Mönkölä, Sanna; Räbinä, Jukka; Rossi, Tuomo

Title: Time-harmonic electromagnetics with exact controllability and discrete exterior calculus

Year: 2023

Version: Published version

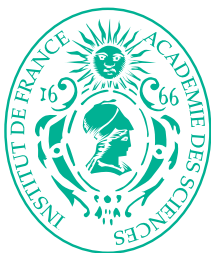Please cite the original version:

Mönkölä, S., Räbinä, J., & Rossi, T. (2023). Time-harmonic electromagnetics with exact controllability and discrete exterior calculus. Comptes Rendus. Mecanique, Online first . https://doi.org/10.5802/crmeca.234

Comptes Rendus

Mécanique

Sanna Mönkölä, Jukka Räbinä and Tuomo Rossi

Time-harmonic electromagnetics with exact controllability and discrete exterior calculus

The scientific legacy of Roland Glowinski / *L'héritage scientifique de Roland Glowinski*

Time-harmonic electromagnetics with exact controllability and discrete exterior calculus

Électromagnétique harmonique temporelle avec contrôlabilité exacte et calcul extérieur discret

Sanna Mönkölä [ORCID],[a]**, Jukka Räbinä** [a] **and Tuomo Rossi** [ORCID],[*],[a]

[a] Faculty of Information Technology, University of Jyväskylä, P.O. Box 35, FI-40014 University of Jyväskylä, Finland
E-mail: tuomo.j.rossi@jyu.fi (T. Rossi)

Abstract. In this paper, we apply the exact controllability concept for time-harmonic electromagnetic scattering. The problem is presented in terms of the differential forms, and the discrete exterior calculus is utilized for spatial discretization. Accordingly, the physical properties of the problem are maintained. Despite we consider time-harmonic problems, we concentrate on transient wave equations treated by the exact controllability approach. Essentially, we use a controlled variation of the asymptotic approach with periodic constraints, in which the time-dependent equation is simulated in time, until the time-harmonic solution is reached.

Résumé. Dans cet article, nous appliquons le concept de contrôlabilité exacte à la dispersion électromagnétique temporelle. Le problème est présenté en termes de formes différentielles et le calcul extérieur discret est utilisé pour la discrétisation spatiale. En conséquence, les propriétés physiques du problème sont maintenues. Bien que nous considérions des problèmes harmoniques temporels, nous nous concentrons sur les équations d'ondes transitoires traitées par l'approche de contrôlabilité exacte. Essentiellement, nous utilisons une variation contrôlée de l'approche asymptotique avec des contraintes périodiques, dans laquelle l'équation dépendant du temps est simulée dans le temps, jusqu'à ce que la solution harmonique temporelle soit atteinte.

Keywords. Maxwell equations, Electromagnetic scattering, Differential forms, Discrete exterior calculus, Exact controllability.

Mots-clés. Équations de Maxwell, Diffusion électromagnétique, Formes différentielles, Calcul extérieur discret, Contrôlabilité exacte.

---

[*] Corresponding author.

1. Introduction

Wave equations are important for modeling acoustic, elastic, electromagnetic, and quantum mechanical systems in different fields of science, engineering, and technology. There has recently been growing interest in differential form -based approaches for considering wave equations (see, e.g., [1–3]). There are several reasons why the framework is a good alternative for the traditional vector field presentation. The metric-free nature of the differential forms allows the construction of differential operators that are independent of the coordinate system [4]. Further, the discrete spaces and exact differential operators can be constructed to mimic their continuous counterparts (see, e.g., [5, 6]). This property also implies that certain properties of the system, such as, energy, are conserved, provided that the scheme is stable.

In this study, we consider time-harmonic electromagnetic waves. We present the Maxwell equations as a first-order system in terms of the differential forms (see, e.g., [7]) for electromagnetic scattering problems. That is, instead of the vector presentation $\mathbf{E} = (E_1, E_2, E_3)$ for the electric field, we present a 1-form $\widetilde{E} = E_1 \, dx^1 + E_2 \, dx^2 + E_3 \, dx^3$, where d is the exterior derivative. Further, the electric flux density is considered, instead of the vector $\mathbf{D} = (D_1, D_2, D_3)$, as a 2-form $\widetilde{D} = D_1 \, dx^2 \wedge dx^3 + D_2 \, dx^3 \wedge dx^1 + D_3 \, dx^1 \wedge dx^2$, where $\wedge$ is a generalization of the cross product, known as the wedge product or exterior product. We also present a 1-form $\widetilde{H}$ for the magnetic field and a 2-form $\widetilde{B}$ for the magnetic flux density.

For the spatial discretization, the discrete counterparts of the variables presented as differential forms are appointed at geometric objects such as points, lines, surfaces, and volumes. We apply, in particular, the discrete exterior calculus (DEC) following the groundwork presented by Marsden and his group [8] and pioneered for electromagnetics simulations by Bossavit and Kettunen [9]. This construction provides, e.g., the conservation of energy, the elimination of non-physical modes, and exact differential operators at the discrete level [10]. The other related approaches include the finite integration technique (FIT), the discrete geometric approach, and mixed finite element techniques with Nédélec and Raviart–Thomas elements (see [11] and the references therein).

From a mathematical point of view, it is convenient to use a four-dimensional (three spatial dimensions and one temporal dimension) space–time presentation. The framework also allows the application of the generalized theories proposed in [12,13]. Still, the four-dimensional system leads to large numerical systems that also require sophisticated computational grids. To demonstrate how the conventional three-dimensional problem is inherited from the generalized wave model, we first present the four-dimensional background at the modeling phase and go on to proceed in time with three-dimensional spatial discretization. Earlier we have presented a numerical scheme for transient electromagnetics with the DEC and high-quality grids [14, 15]. In this paper, we systematically apply and test these techniques for simulating time-harmonic electromagnetic scattering.

We follow the exact controllability concept (see, e.g., [16]) and solve the time-harmonic problem by using the model presented in the time domain. This concept has a history dating back to the early 1990s, when Glowinski *et al.* (see [17–19]) first considered a numerical method based on it. Its first application in three-dimensional electromagnetics was, to our knowledge, presented in the INRIA report [20]. The drawback of the approach was that it used H^1-conforming finite elements, rendering it applicable only to limited classes of problems due to spurious modes that can arise in the numerical solution. Additional computational costs are due to the second-order formulation of the Maxwell's equations that was used, leading to slower convergence and the need for preconditioning of the minimization process, since the energy space is not of L^2-type.

To improve the methodology, Glowinski and Rossi [21] considered the wave equation as a first-order system, and they derived the associated exact controllability scheme. The main benefit of

their approach is that the system's energy space, where the minimization is realized, is of L^2-type, and the minimization converges without preconditioning. The drawback, however, is the need to use mixed methods (e.g. Raviart–Thomas finite elements [22]) in discretizing the problem. Recently, a first-order form based on a discontinuous Galerkin method was developed for the three-dimensional Maxwell case [23].

Instead of using mixed finite elements, another approach, based on DEC, started to progress with the PhD thesis of Räbinä [24]. The idea for his thesis arose from the theoretical article [25]. Räbinä also considered exact controllability techniques for the computation of time-harmonic waves. Several improvements for the time integration of the Maxwell's system, such as adaptive local time-stepping, harmonic Hodge star approximation, and spatial tilings inspired by crystallography, were then introduced in [14]. In [15], the DEC approach was further generalized to a class of wave problems covering acoustics, elastodynamics, electromagnetism, and even quantum mechanics (the Weyl equation). Further applications in quantum mechanics were then considered in [26–28]. The systematization of scientific software development covering fundamental conservation laws was sketched in [29], and a generic category-theoretic framework of space–time linear wave phenomena was finally proposed by [30] in 2022. Such formalisms allow, e.g., moving and deforming computational domains [29]. Another research track considers higher-order discrete exterior calculus involving higher order Whitney forms and novel Hodge star formulations [31–33].

The exact controllability approach was extensively studied in the late 2000s and early 2010s by Mönkölä *et al.* In particular, higher-order spectral element discretizations and fluid-structure interaction problems were considered in [34–36]. The approach was recently extended to three-dimensional visco-elastic equations [37]. Essentially, the approach is a controlled variation of the asymptotic approach with periodic constraints, in which the time-dependent equation is simulated in time until the time-harmonic solution is reached. The time discretization is realized with a staggered leapfrog-type scheme with asynchronous time steps (see, [14,38,39]). In practice, the residual of the exact controllability algorithm defines at each iteration how far the solution is from a periodic one. It also gives an an impulse to the system to accelerate the convergence rate. Roughly speaking, the number of computational operations grows linearly with the number of degrees of freedom involved in the spatial discretization.

The rest of this article is organized as follows. In Section 2, we present the four-dimensional differential form formulation. The model is simplified into separate time and space dimensions in Section 3, where we also carry out discretization. To eliminate discretization errors, we adjust the scheme for time-harmonic problems with spatial and temporal corrections. This type of strategy has been used to improve the accuracy of time discretization in electromagnetics, e.g., by Ma and Chen [40] and Appelö *et al.* [41]. The spatial correction term is derived within the discrete exterior calculus that we use for space discretization, and the temporal correction term arises from adapting the leapfrog time discretization to time-harmonic equations. Nevertheless, both correction terms can be encapsulated into discrete Hodge operators. In Section 4, we focus on a time-harmonic problem and consider how it can be solved efficiently in the time domain with the exact controllability method. The problem is reformulated as a least-squares optimization problem that is solved by the conjugate gradient algorithm. In Section 5, we apply the approach to three-dimensional electromagnetic scattering problems and test the performance of the method with several types of computational meshes. The concluding remarks are presented in Section 6.

2. Model

We consider a linear combination of the differential forms in the four-dimensional Euclidean space $(x_0, x_1, x_2, x_3)^T$ as $\tilde{F} = \tilde{u}_1 + \tilde{u}_2 \, dx^0 + \tilde{u}_3 \, dx^1 + \tilde{u}_4 \, dx^2 + \tilde{u}_5 \, dx^3 + \tilde{u}_6 (dx^0 \wedge dx^1) + \tilde{u}_7 (dx^0 \wedge dx^2) +$

$\tilde{u}_8(dx^0 \wedge dx^3) + \tilde{u}_{11}(dx^2 \wedge dx^3) + \tilde{u}_{10}(dx^3 \wedge dx^1) + \tilde{u}_9(dx^1 \wedge dx^2) + \tilde{u}_{14}(dx^0 \wedge dx^2 \wedge dx^3) + \tilde{u}_{13}(dx^0 \wedge dx^3 \wedge dx^1) + \tilde{u}_{12}(dx^0 \wedge dx^1 \wedge dx^2) + \tilde{u}_{15}(dx^1 \wedge dx^2 \wedge dx^3) + \tilde{u}_{16}(dx^0 \wedge dx^1 \wedge dx^2 \wedge dx^3)$, where the coefficients $\tilde{u}_i$, $i = 1,\dots,16$ are scalar-valued. The basis 1-forms are the coordinate differentials dx^0, dx^1, dx^2, and dx^3, and higher order basis k-forms, $k = 2,3,4$, are constructed as exterior products of k basis 1-forms, such that, $dx^i \wedge dx^i = 0$ and $dx^i \wedge dx^j = -dx^j \wedge dx^i$. This formulation allows us to present a set of linear models with the first-order differential operator in a short form,

$$(\boldsymbol{d} + \boldsymbol{\delta})\tilde{F} = \tilde{J}, \tag{1}$$

where $\boldsymbol{d} = \sum_{i=0}^{3}(dx^i \partial_i \wedge)$ is the exterior derivative, $\boldsymbol{\delta}$ is the coderivative of $\boldsymbol{d}$, and $\tilde{J}$ is a source term presented as a linear combination of the differential forms. Accordingly, Equation (1) is equivalent to the system

$$
\begin{pmatrix}
-\partial_0 & & & & & \nabla \cdot & & \\
& -\partial_0 & & \nabla \cdot & & & & \\
& & -\partial_0 & & -\nabla \times & & & \nabla \\
& & & -\partial_0 & -\nabla \times & & & \nabla \\
& \nabla & & \nabla \times & -\partial_0 & & & \\
\nabla & & \nabla \times & & & -\partial_0 & & \\
& & & \nabla \cdot & & & -\partial_0 & \\
& & \nabla \cdot & & & & & -\partial_0
\end{pmatrix}
\begin{pmatrix}
\tilde{u}_{15} \\
\tilde{u}_{16} \\
\tilde{\boldsymbol{u}}_3 \\
\tilde{\boldsymbol{u}}_6 \\
\tilde{\boldsymbol{u}}_{11} \\
\tilde{\boldsymbol{u}}_{14} \\
\tilde{u}_1 \\
\tilde{u}_2
\end{pmatrix}
=
\begin{pmatrix}
-\tilde{b}_{16} \\
\tilde{b}_{15} \\
-\tilde{\boldsymbol{b}}_6 \\
\tilde{\boldsymbol{b}}_3 \\
-\tilde{\boldsymbol{b}}_{14} \\
\tilde{\boldsymbol{b}}_{11} \\
-\tilde{b}_2 \\
\tilde{b}_1
\end{pmatrix},
\tag{2}
$$

where

$$\tilde{\boldsymbol{u}}_3 := \begin{pmatrix} \tilde{u}_3 \\ \tilde{u}_4 \\ \tilde{u}_5 \end{pmatrix}, \quad \tilde{\boldsymbol{u}}_6 := \begin{pmatrix} \tilde{u}_6 \\ \tilde{u}_7 \\ \tilde{u}_8 \end{pmatrix}, \quad \tilde{\boldsymbol{u}}_{11} := \begin{pmatrix} \tilde{u}_{11} \\ \tilde{u}_{10} \\ \tilde{u}_9 \end{pmatrix}, \quad \text{and} \quad \tilde{\boldsymbol{u}}_{14} := \begin{pmatrix} \tilde{u}_{14} \\ \tilde{u}_{13} \\ \tilde{u}_{12} \end{pmatrix},$$

and

$$\tilde{\boldsymbol{b}}_3 := \begin{pmatrix} \tilde{b}_3 \\ \tilde{b}_4 \\ \tilde{b}_5 \end{pmatrix}, \quad \tilde{\boldsymbol{b}}_6 := \begin{pmatrix} \tilde{b}_6 \\ \tilde{b}_7 \\ \tilde{b}_8 \end{pmatrix}, \quad \tilde{\boldsymbol{b}}_{11} := \begin{pmatrix} \tilde{b}_{11} \\ \tilde{b}_{10} \\ \tilde{b}_9 \end{pmatrix}, \quad \text{and} \quad \tilde{\boldsymbol{b}}_{14} := \begin{pmatrix} \tilde{b}_{14} \\ \tilde{b}_{13} \\ \tilde{b}_{12} \end{pmatrix}.$$

We interpret ∂_0 as a time derivative and ∇, $\nabla \cdot$, and $\nabla \times$ as three-dimensional gradient, divergence, and curl operators, respectively. By the choice $\tilde{u}_1 = \tilde{u}_2 = \tilde{u}_{15} = \tilde{u}_{16} = 0$, rows 1, 2, 5, and 6 of Equation (2) give the complete set of the Maxwell equations with the magnetic field strength $\tilde{\boldsymbol{u}}_3 = (H_1, H_2, H_3)^T$, the electric field strength $\tilde{\boldsymbol{u}}_6 = (E_1, E_2, E_3)^T$, the magnetic flux density $\tilde{\boldsymbol{u}}_{11} = -(B_1, B_2, B_3)^T$, and the electric flux density $\tilde{\boldsymbol{u}}_{14} = (D_1, D_2, D_3)^T$, respectively. The magnetic current density is $-\tilde{\boldsymbol{b}}_{14}$, the electric current density is $-\tilde{\boldsymbol{b}}_{11}$, and magnetic and electric charges are modeled by $-\tilde{u}_{15}$ and $-\tilde{u}_{16}$. A Maxwell-like system is also obtained from rows 3, 4, 7, and 8 of Equation (2).

We return to Equation (1) and consider

$$\tilde{F} = \widetilde{H} + dx^0 \wedge \widetilde{E} - \widetilde{B} + dx^0 \wedge \widetilde{D}, \tag{3}$$

$$\tilde{J} = -\widetilde{J}_E - dx^0 \wedge \widetilde{J}_H - \widetilde{J}_{\rho_H} - dx^0 \wedge \widetilde{J}_{\rho_E} - \widetilde{J}_B - dx^0 \wedge \widetilde{J}_D - \widetilde{J}_{\rho_D} - dx^0 \wedge \widetilde{J}_{\rho_B}, \tag{4}$$

where respectively, electric and magnetic field strengths are represented by spatial 1-forms $\widetilde{E} = E_1 dx^1 + E_2 dx^2 + E_3 dx^3$ and $\widetilde{H} = H_1 dx^1 + H_2 dx^2 + H_3 dx^3$, electric and magnetic flux densities and electric and magnetic current densities by spatial 2-forms $\widetilde{D} = D_1 dx^2 \wedge dx^3 + D_2 dx^3 \wedge dx^1 + D_3 dx^1 \wedge dx^2$, $\widetilde{B} = B_1 dx^2 \wedge dx^3 + B_2 dx^3 \wedge dx^1 + B_3 dx^1 \wedge dx^2$, $\widetilde{J}_E = J_{E1}(dx^2 \wedge dx^3) + J_{E2}(dx^3 \wedge dx^1) + J_{E3}(dx^1 \wedge dx^2)$, and $\widetilde{J}_H = J_{H1}(dx^2 \wedge dx^3) + J_{H2}(dx^3 \wedge dx^1) + J_{H3}(dx^1 \wedge dx^2)$, and electric and magnetic charges, ρ_E and ρ_H, by spatial 3-forms $\widetilde{J}_{\rho_E} = \rho_E(dx^1 \wedge dx^2 \wedge dx^3)$ and

$\widetilde{J}_{\rho_H} = \rho_H(dx^1 \wedge dx^2 \wedge dx^3)$. Further, in Equation (3), there are also source forms for current densities and charges corresponding to the dual components of the electric and magnetic ones, referred to with subscripts *B* and *D*, respectively. From the choices made above, we get from Equation (1) to the differential form formulations

$$\begin{cases} \boldsymbol{d}\widetilde{H} - \partial_0\widetilde{D} = -\widetilde{J}_E, \\ dx^0 \wedge (\boldsymbol{d}\widetilde{E} - \boldsymbol{d}\widetilde{B}) = -dx^0 \wedge \widetilde{J}_H, \\ -dx^0 \wedge \boldsymbol{d}\widetilde{B} = -dx^0 \wedge \widetilde{J}_{\rho_H}, \\ -dx^0 \wedge \boldsymbol{d}\widetilde{D} = -dx^0 \wedge \widetilde{J}_{\rho_E}, \end{cases} \qquad (5)$$

$$\begin{cases} -\star(dx^0 \wedge \boldsymbol{d}\widetilde{H}) = -\star(dx^0 \wedge \widetilde{J}_{\rho_B}), \\ -\star(dx^0 \wedge \boldsymbol{d}\widetilde{E}) = -\star(dx^0 \wedge \widetilde{J}_{\rho_D}), \\ \star(dx^0 \wedge (\boldsymbol{d}\widetilde{B} - \boldsymbol{d}\widetilde{E})) = -\star(dx^0 \wedge \widetilde{J}_D), \\ \star(\boldsymbol{d}\widetilde{D} - \partial_0\widetilde{H}) = -\star\widetilde{J}_B, \end{cases} \qquad (6)$$

where $\star$ is the Hodge star operator. The systems (5) and (6) are dual to each other, and in what follows, we proceed with Equation (5) in separate space and time dimensions. For further information on differential forms in electromagnetics, the reader is referred to, e.g., [42–44] and the references therein.

3. Discretization

The quality of the discrete model, based on the structure of the computational grid, has a significant impact on the efficiency of the method. As presented in [14], we generate partly-structured non-uniform polygonal grids imitating the close packing in crystal lattices and discretize the operators in the spatial domain with the DEC.

We discretize the three-dimensional spatial domain by a pair of primal and dual grids. The elements of a grid are called *k*-cells, where $k = 0, 1, 2, 3$ is the dimension of the cell. Basically, a *k*-cell is an oriented, convex, polygon style object, and it is defined in a recursive manner by a list of $k-1$-cells. A 0-cell (node) is a vertex. A 1-cell (edge) is defined as a line segment between two 0-cells and oriented from the first to the second node of the list. A 2-cell (face) is a convex polygon surrounded by a finite set of edges. The boundary edges are presented with counterclockwise orientation, also providing, the orientation of the face element. A 3-cell (body) is a convex polyhedron surrounded by a finite set of faces. The grid construction has a crucial role in the accuracy of the method.

In practice, we generate a partly structured grid that consists of structured areas separated by unstructured ones. The approach allows us to model boundaries as accurately as with fully unstructured grids, and it is also possible to modify element sizes inside the domain. The grid generation is based on the Delaunay triangulation (see [45]). With the help of a Voronoi diagram, it is possible to create sophisticated polyhedral grids to fill the structured parts of the grid. By maintaining the number of unstructured elements at a relatively low level, the grid generation process is considerably sped up. By constructing the dual elements that are orthogonal to the corresponding primal elements, we get diagonal discrete Hodge operators, providing a significant saving in computing time.

3.1. *Discrete differential forms*

The discrete differential *k*-forms (*k*-cochains) are variables associated by the de Rham map with the *k*-cells in the grid (see, e.g., [24, 46]) that, in the three-dimensional construction, are 1-cells (edges) and 2-cells (faces). We denote the *i*th edge of the grid by e_i, $i = 1, \ldots, n_e$, and the *j*th face by f_j, $j = 1, \ldots, m_f$, and the corresponding dual elements by f_i^* and e_j^*, respectively. Accordingly,

the components of the vector-valued discrete differential 1-forms E and H, presenting the discretized electric and magnetic fields and associated with the primal and dual edges, are

$$E_i = \int_{e_i} \widetilde{E}, \quad H_j = \int_{e_j^*} \widetilde{H}, \quad i = 1, \dots, n_e, j = 1, \dots, m_f. \tag{7}$$

Respectively, D and B present the discretized electric and magnetic fluxes, such that,

$$D_i = \int_{f_i^*} \widetilde{D}, \quad B_j = \int_{f_j} \widetilde{B}, \quad i = 1, \dots, n_e, j = 1, \dots, m_f, \tag{8}$$

are the discrete differential 2-forms associated with the dual and primal faces of the grid elements. Also, the vectors for source forces, J_E and J_H, are considered as discrete differential 2-forms

$$J_{E_i} = \int_{f_i^*} \widetilde{J}_E, \quad J_{H_j} = \int_{f_j} \widetilde{J}_H, \quad i = 1, \dots, n_e, j = 1, \dots, m_f, \tag{9}$$

associated with the dual and primal faces.

The relation between the discrete 1-forms E and H and discrete 2-forms D and B is presented by the constitutive equations

$$D = \bigstar_\epsilon E, \quad B = \bigstar_\mu H, \tag{10}$$

where the discrete Hodge star operators $\bigstar_\epsilon$ and $\bigstar_\mu$ cover the material properties, permittivity ϵ and permeability μ, respectively, and the metric properties of the space or coordinate system. In this paper, the discrete Hodge star operators are diagonal matrices based on the orthogonality of the primal and dual elements and defined as

$$\bigstar_\alpha = \frac{|f|}{|e||f \diamond e|} \int_{f \diamond e} \alpha \mathbf{n}_e \cdot \mathbf{n}_e dv, \tag{11}$$

where $\mathbf{n}_e$ is the unit orientation vector of edge e, and $f \diamond e$ is a convex hull including both e and f. The ith diagonal component of $\bigstar_\epsilon$ is composed by setting $\alpha = \epsilon, e = e_i$, and $f = f_i^*$ in Equation (11). The jth diagonal component of $\bigstar_\mu$ is composed by setting $\alpha = \mu, e = e_j^*$, and $f = f_j$ in Equation (11).

The key component of the discrete exterior calculus is the discrete exterior derivative, or incidence matrix, d representing the neighboring relations and relative orientations of the primal edges and faces. We use the notation d_1 to emphasize that in this case, the discrete exterior derivative operates discrete 1-forms. The matrix entry, $d_{1_{ji}}$, is non-zero if and only if the edge e_i is included in the boundary of the face f_j. Further, the non-zero entries have the value ± 1, indicating the relative orientation defined by counter-clockwise circulation.

With the notations presented above, the electromagnetic system after space discretization in a three-dimensional domain Ω is

$$\bigstar_\epsilon \frac{\partial E}{\partial t} - d_1^T H = -J_E, \quad \text{in } \Omega \times [0, \tau], \tag{12}$$

$$\bigstar_\mu \frac{\partial H}{\partial t} + d_1 E = -J_H, \quad \text{in } \Omega \times [0, \tau], \tag{13}$$

with the initial conditions, $E(0)$ and $H(0)$, set at the initial time 0. The final state is considered at the final time τ. By denoting

$$\mathsf{M} = \begin{pmatrix} \bigstar_\epsilon & 0 \\ 0 & \bigstar_\mu \end{pmatrix}, \quad \mathsf{K} = \begin{pmatrix} 0 & -d_1^T \\ d_1 & 0 \end{pmatrix}, \tag{14}$$

we can write Equations (12)–(13) with the initial conditions as

$$(\mathsf{M}\partial_0 + \mathsf{K}) \begin{pmatrix} E \\ H \end{pmatrix} = - \begin{pmatrix} J_E \\ J_H \end{pmatrix}, \quad \text{in } \Omega \times [0, \tau], \tag{15}$$

$$\begin{pmatrix} E(0) \\ H(0) \end{pmatrix} = \begin{pmatrix} E^0 \\ H^0 \end{pmatrix}, \quad \text{in } \Omega, \tag{16}$$

the solution of which, at time t, is

$$\begin{pmatrix} E(t) \\ H(t) \end{pmatrix} = e^{-t M^{-1} K} \begin{pmatrix} E^0 \\ H^0 \end{pmatrix} - \int_0^t e^{-(t-s)M^{-1}K} M^{-1} \begin{pmatrix} J_E(s) \\ J_H(s) \end{pmatrix} ds, \tag{17}$$

where

$$
\begin{aligned}
e^{-t M^{-1} K} &= I + \begin{pmatrix} 0 & \bigstar_\epsilon^{-1} d_1^T t \\ -\bigstar_\mu^{-1} d_1 t & 0 \end{pmatrix} + \frac{\begin{pmatrix} 0 & \bigstar_\epsilon^{-1} d_1^T t \\ -\bigstar_\mu^{-1} d_1 t & 0 \end{pmatrix}^2}{2!} + \frac{\begin{pmatrix} 0 & \bigstar_\epsilon^{-1} d_1^T t \\ -\bigstar_\mu^{-1} d_1 t & 0 \end{pmatrix}^3}{3!} + \frac{\begin{pmatrix} 0 & \bigstar_\epsilon^{-1} d_1^T t \\ -\bigstar_\mu^{-1} d_1 t & 0 \end{pmatrix}^4}{4!} + \dots \\
&= \begin{pmatrix} \cos\left(\left(\bigstar_\epsilon^{-1} d_1^T \bigstar_\mu^{-1} d_1\right)^{\frac12} t\right) & \bigstar_\epsilon^{-1} d_1^T \left(\bigstar_\mu^{-1} d_1 \bigstar_\epsilon^{-1} d_1^T\right)^{-\frac12} \sin\left(\left(\bigstar_\mu^{-1} d_1 \bigstar_\epsilon^{-1} d_1^T\right)^{\frac12} t\right) \\ -\bigstar_\mu^{-1} d_1 \left(\bigstar_\epsilon^{-1} d_1^T \bigstar_\mu^{-1} d_1\right)^{-\frac12} \sin\left(\left(\bigstar_\epsilon^{-1} d_1^T \bigstar_\mu^{-1} d_1\right)^{\frac12} t\right) & \cos\left(\left(\bigstar_\mu^{-1} d_1 \bigstar_\epsilon^{-1} d_1^T\right)^{\frac12} t\right) \end{pmatrix}. \tag{18}
\end{aligned}
$$

The derivative of the total energy

$$\frac{d}{dt} \mathscr{E}(E, H) = E^T \bigstar_\epsilon \partial_0 E + H^T \bigstar_\mu \partial_0 H = -(E^T J_E + H^T J_H) \tag{19}$$

is obtained by multiplying Equation (15) from the left by $(E^T H^T)$. The right-hand side of Equation (19) includes the source functions set on the absorbing boundary or layer, such as the Silver–Müller boundary condition [47] or perfectly matched layer (PML) [48]. By assuming them to be of the forms $J_E = \bigstar_{\sigma_E} E$ and $J_H = \bigstar_{\sigma_H} H$, where σ_E and σ_H present the electric and magnetic conductivities, respectively, we get $(d/dt)\mathscr{E}(E, H) = -(E^T \bigstar_{\sigma_E} E + H^T \bigstar_{\sigma_H} H) \le 0$, implying that the energy is conserved or dissipated as the waves are absorbed from the domain. The total energy of the electromagnetic system is

$$\mathscr{E}(E, H) = \tfrac{1}{2}(E^T \bigstar_\epsilon E + H^T \bigstar_\mu H). \tag{20}$$

3.2. *Spatial harmonic correction*

To improve the accuracy of the simulations involving time-harmonic waves with the time-dependence of the form $e^{i\omega t}$, where ω is the angular frequency and i is the imaginary unit, we formulate spatially harmonic corrections for the discrete Hodge operators. Since the electromagnetic wave speed is $c = 1/\sqrt{\mu\epsilon}$, we can present time t as distance multiplied by $\sqrt{\mu\epsilon}$. From this basis, the concept of spatial correction is based on obtaining the components of E and H in Equation (7) by integrating over $\hat{E}e^{i\omega t}$ and $\hat{H}e^{i\omega t}$, with complex-valued $\hat{E}$ and $\hat{H}$, instead of integrating over $\widetilde{E}$ and $\widetilde{H}$. Respectively, in Equations (8) we integrate over $\epsilon_i \hat{E} e^{i\omega t}$ and $\mu_j \hat{H} e^{i\omega t}$, instead of $\widetilde{D}$ and $\widetilde{B}$, to obtain the components of D and B. Accordingly, by minimizing the squared norm of errors based on the constitutive equations, we find spatially harmonic discrete Hodge star operators $\bigstar_\epsilon^{\text{spat}}$ and $\bigstar_\mu^{\text{spat}}$ to satisfy the constitutive equations. These are diagonal matrices with the diagonal components

$$\bigstar_{\epsilon_i}^{\text{spat}} = \bigstar_{\epsilon_i} \kappa_i, i = 1, \dots, n_e, \quad \bigstar_{\mu_j}^{\text{spat}} = \bigstar_{\mu_j} \kappa_j^*, \quad j = 1, \dots, m_f, \tag{21}$$

where the spatial correction terms, κ_i and κ_j^*, are

$$\kappa_i = \left(\frac{1 - \frac{\kappa_{f*}}{5} + \frac{\kappa_{f*}^2}{56}}{1 - \frac{\kappa_{f*}}{10} - \frac{\kappa_e}{120} + \frac{\kappa_{f*}^2}{280} + \frac{\kappa_{f*}\kappa_e}{1680} + \frac{\kappa_e^2}{22,400}} \right), \quad \kappa_j^* = \left(\frac{1 - \frac{\kappa_f}{5} + \frac{\kappa_f^2}{56}}{1 - \frac{\kappa_f}{10} - \frac{\kappa_{e*}}{120} + \frac{\kappa_f^2}{280} + \frac{\kappa_f\kappa_{e*}}{1680} + \frac{\kappa_{e*}^2}{22,400}} \right),$$

with $\kappa_e = \omega^2 \epsilon\mu |e_i|^2$, $\kappa_{f*} = \omega^2 \epsilon\mu r_{f_i^*}^2$, $\kappa_{e*} = \omega^2 \epsilon\mu |e_j^*|^2$, and $\kappa_f = \omega^2 \epsilon\mu r_{f_j}^2$ and the squared radii of the faces f_i^* and f_j, $r_{f_i^*}^2$ and $r_{f_j}^2$, respectively (see [14, 24]). Respectively,

$$\bigstar_{\sigma_{E_i}}^{\text{spat}} = \bigstar_{\sigma_{E_i}} \kappa_i, \quad i = 1, \dots, n_e, \quad \bigstar_{\sigma_{H_j}}^{\text{spat}} = \bigstar_{\sigma_{H_j}} \kappa_j^*, \quad j = 1, \dots, m_f. \tag{22}$$

The larger the grid elements, the more advantages are gained by replacing $\bigstar_\epsilon$ by $\bigstar_\epsilon^{\text{spat}}$, $\bigstar_\mu$ by $\bigstar_\mu^{\text{spat}}$, $\bigstar_{\sigma_E}$ by $\bigstar_{\sigma_E}^{\text{spat}}$, and $\bigstar_{\sigma_H}$ by $\bigstar_{\sigma_H}^{\text{spat}}$ in time-harmonic simulations.

3.3. *Exact time-stepping*

For time-harmonic waves, we assume that $E^{k+(1/2)} = \mathrm{Re}(\hat{E}\exp(-\mathrm{i}\omega(t^k + (\Delta t/2))))$ and $H^k = \mathrm{Re}(\hat{H}\exp(-\mathrm{i}\omega t^k))$, where $\hat{E}$ and $\hat{H}$ are complex-valued, to eliminate the approximation error of the time discretization. Essentially, for uniform space discretization, we multiply M by the correction factor $((2\Delta t/\omega)\sin(\omega\Delta t/2))^{-1}$ and K by the correction factor $(\cos(\omega\Delta t/2s))^{-1}$, where s is the timestep size factor. For non-uniform space discretization, we obtain the exact time stepping scheme with the following update formulas:

$$E^{k+\frac{1}{2}} = E^{k-\frac{1}{2}} + \left(\frac{1}{\frac{2}{\omega}\sin\frac{\omega\Delta t}{2s}} \bigstar_\epsilon^{\mathrm{spat}} + \frac{1}{2\cos\frac{\omega\Delta t}{2s}} \bigstar_{\sigma_E}^{\mathrm{spat}} \right)^{-1} \left(d_1^T H^k - \frac{1}{\cos\frac{\omega\Delta t}{2s}} \bigstar_{\sigma_E}^{\mathrm{spat}} E^{k-\frac{1}{2}} + F_1^k \right),$$
(23)

$$H^{k+1} = H^k + \left(\frac{1}{\frac{2}{\omega}\sin\frac{\omega\Delta t}{2s}} \bigstar_\mu^{\mathrm{spat}} + \frac{1}{2\cos\frac{\omega\Delta t}{2s}} \bigstar_{\sigma_H}^{\mathrm{spat}} \right)^{-1} \left(d_1 E^{k+\frac{1}{2}} - \frac{1}{\cos\frac{\omega\Delta t}{2s}} \bigstar_{\sigma_H}^{\mathrm{spat}} H^k + F_2^{k+\frac{1}{2}} \right),$$
(24)

where $k = 0,\ldots,N-1$. The use of the varying timestep size factor s in non-uniform time-stepping is described in [49].

For simplicity, we present the system of Equations (23)–(24) with the initial conditions as

$$S(\mathbf{e}, U(\mathbf{e})) := \begin{pmatrix} I & & & & \\ \mathscr{C} & \mathscr{D} & & & \\ & \mathscr{C} & \mathscr{D} & & \\ & & \ddots & \ddots & \\ & & & \mathscr{C} & \mathscr{D} \\ & & & & \mathscr{C} & \mathscr{D} \end{pmatrix} \begin{pmatrix} U^0 \\ U^1 \\ \vdots \\ \vdots \\ U^{N-1} \\ U^N \end{pmatrix} - \begin{pmatrix} I \\ 0 \\ \vdots \\ \vdots \\ 0 \\ 0 \end{pmatrix} \mathbf{e} + \begin{pmatrix} 0 \\ \mathscr{F}^0 \\ \vdots \\ \vdots \\ \mathscr{F}^{N-2} \\ \mathscr{F}^{N-1} \end{pmatrix} = 0,$$
(25)

where $U^k = (E^{k-(1/2)}, H^k)^T = (E(t^k - (\Delta t/2)), H(t^k))^T$, $t^k = t^0 + k\Delta t$, $k = 0,\ldots,N$, $U = (U^0,\ldots,U^N)^T$, and I is the identity matrix. The initial conditions are $\mathbf{e} = (\mathbf{e}_0, \mathbf{e}_1)^T = (E^{-(1/2)}, H^0)^T$, $\mathscr{F}^k = (F_1^k, F_2^{k+(1/2)})^T$, and $k = 0,\ldots,N-1$, and the matrix blocks $\mathscr{C}$ and $\mathscr{D}$ are given by

$$\mathscr{C} = \begin{pmatrix} \left(\frac{1}{\Delta t}\bigstar_\epsilon^{\mathrm{har}} + \frac{1}{2}\bigstar_{\sigma_E}^{\mathrm{har}}\right)^{-1} \bigstar_{\sigma_E}^{\mathrm{har}} - I & -\left(\frac{1}{\Delta t}\bigstar_\epsilon^{\mathrm{har}} + \frac{1}{2}\bigstar_{\sigma_E}^{\mathrm{har}}\right)^{-1} d_1^T \\ 0 & \left(\frac{1}{\Delta t}\bigstar_\mu^{\mathrm{har}} + \frac{1}{2}\bigstar_{\sigma_H}^{\mathrm{har}}\right)^{-1} \bigstar_{\sigma_H}^{\mathrm{har}} - I \end{pmatrix},$$
(26)

$$\mathscr{D} = \begin{pmatrix} I & 0 \\ \left(\frac{1}{\Delta t}\bigstar_\mu^{\mathrm{har}} + \frac{1}{2}\bigstar_{\sigma_H}^{\mathrm{har}}\right)^{-1} d_1 & I \end{pmatrix},$$
(27)

where

$$\bigstar_\epsilon^{\mathrm{har}} = \frac{\Delta t}{\frac{2}{\omega}\sin\frac{\omega\Delta t}{2s}} \bigstar_\epsilon^{\mathrm{spat}} = \frac{\kappa_i \Delta t}{\frac{2}{\omega}\sin\frac{\omega\Delta t}{2s}} \bigstar_{\epsilon_i}, \quad \bigstar_\mu^{\mathrm{har}} = \frac{\Delta t}{\frac{2}{\omega}\sin\frac{\omega\Delta t}{2s}} \bigstar_\mu^{\mathrm{spat}} = \frac{\kappa_j^* \Delta t}{\frac{2}{\omega}\sin\frac{\omega\Delta t}{2s}} \bigstar_{\mu_j},$$
(28)

$$\bigstar_{\sigma_E}^{\mathrm{har}} = \frac{1}{\cos\frac{\omega\Delta t}{2s}} \bigstar_{\sigma_E}^{\mathrm{spat}} = \frac{\kappa_i}{\cos\frac{\omega\Delta t}{2s}} \bigstar_{\sigma_{E_i}}, \quad \bigstar_{\sigma_H}^{\mathrm{har}} = \frac{1}{\cos\frac{\omega\Delta t}{2s}} \bigstar_{\sigma_H}^{\mathrm{spat}} = \frac{\kappa_j^*}{\cos\frac{\omega\Delta t}{2s}} \bigstar_{\sigma_{H_j}},$$
(29)

are the discrete harmonic Hodge operators that include both the spatial and temporal correction to improve the accuracy of time-harmonic simulations. Furthermore, the structure of Equation (25) is exactly the same as if we had done the conventional leapfrog time discretization. That is, replacing the discrete harmonic Hodge operators with the conventional Yee's Hodge operators (without correction terms), we get the the conventional leapfrog time discretization of the system

discretized in the space domain by the discrete exterior calculus. Accordingly, it is also straight-forward to update an existing computer code with the correction terms. Based on Equation (25), we can solve the system's state at time $t^0 + k\Delta t$ as $U^k = -\mathscr{D}^{-1}(\mathscr{C}U^{k-1} + \mathscr{F}^{k-1})$ for $k = 1,\ldots,N$. Thus, by denoting $\mathsf{Q} = -\mathscr{D}^{-1}\mathscr{C}$, the final state is

$$U^N = \mathsf{Q}^N U^0 - \mathsf{Q}^{N-1}\mathscr{D}^{-1}\mathscr{F}^0 - \mathsf{Q}^{N-2}\mathscr{D}^{-1}\mathscr{F}^1 \cdots - \mathsf{Q}\mathscr{D}^{-1}\mathscr{F}^{N-2} - \mathscr{D}^{-1}\mathscr{F}^{N-1}. \tag{30}$$

4. Exact controllability scheme

Our main interest is in the solution of the time-harmonic problem

$$(-\mathsf{M}\mathrm{i}\omega + \mathsf{K})\begin{pmatrix}\hat{E}\\\hat{H}\end{pmatrix} = -\begin{pmatrix}\hat{J}_E\\\hat{J}_H\end{pmatrix}, \quad \text{in } \Omega, \tag{31}$$

where ω is the angular frequency and i is the imaginary unit. That is, the solution of Equation (31) is periodic in time with a fixed frequency $f = \omega/2\pi$. At first sight, it would be tempting to solve such a problem in the frequency domain by strictly following Equation (31). In principle, the other alternative is the asymptotic approach, i.e., integration in the time domain. If there are non-convex scatterers involved in the simulations, the plain time integration converges slowly towards a time-harmonic solution. This issue is tackled by the exact controllability method pioneered by Bristeau *et al.* [16, 18], which is essentially a controlled version of the asymptotic approach with periodic constraints. In what follows, we harness the exact controllability method to accelerate the convergence rate of the asymptotic approach.

4.1. *Semidiscrete approach*

We consider the time period $\tau = 2\pi/\omega$. By definition, the initial solution of a time-harmonic problem is equal to the solution after one time period. Therefore, based on the semidiscrete presentation for the final state in Equation (17), we can write

$$\begin{pmatrix}E(\tau)\\H(\tau)\end{pmatrix} - \begin{pmatrix}E(0)\\H(0)\end{pmatrix} = \mathsf{C}\mathbf{e} + \mathsf{f} = 0, \tag{32}$$

where $\mathsf{C} = (\mathrm{e}^{-\tau\mathsf{M}^{-1}\mathsf{K}} - I)$, I is an identity matrix, $\mathbf{e} = (E^0, H^0)^T$ is the initial condition, and

$$\mathsf{f} = -\int_0^\tau \mathrm{e}^{-(\tau-s)\mathsf{M}^{-1}\mathsf{K}}\mathsf{M}^{-1}\begin{pmatrix}J_E(s)\\J_H(s)\end{pmatrix}.$$

The final state $(E(\tau), H(\tau))^T$ is a function of initial conditions. In practice, we can catch the solution of Equation (31) by solving the corresponding linear system

$$\mathsf{C}\mathbf{e} = -\mathsf{f}, \tag{33}$$

where C is a non-symmetric and non-self-adjoint coefficient matrix. By multiplying (33) by the adjoint of the coefficient matrix C^*, we get a linear system

$$\mathsf{C}^*\mathsf{C}\mathbf{e} = -\mathsf{C}^*\mathsf{f}, \tag{34}$$

which has the symmetric and positive definite coefficient matrix. By applying, instead of the standard inner product, the weighted inner product defined as $\langle A, B\rangle = A^T\mathsf{M}B$, where M is symmetric and positive definite matrix, we get the linear system

$$\mathsf{C}^*\mathsf{M}\mathsf{C}\mathbf{e} = -\mathsf{C}^*\mathsf{M}\mathsf{f}. \tag{35}$$

4.2. *Fully discrete approach*

Also at the fully discrete level the exact controllability scheme for computing a time-harmonic solution involves finding such initial conditions that the solution after one time period coincides with the initial conditions. Hence, after time-discretization, we use Equation (30) to present the solution after one time period, set it equal to the initial solution, i.e.,

$$U^N - U^0 = (\mathsf{Q}^N - I)U^0 - \mathsf{Q}^{N-1}\mathscr{D}^{-1}\mathscr{F}^0 - \mathsf{Q}^{N-2}\mathscr{D}^{-1}\mathscr{F}^1 \cdots - \mathsf{Q}\mathscr{D}^{-1}\mathscr{F}^{N-2} - \mathscr{D}^{-1}\mathscr{F}^{N-1} = 0, \quad (36)$$

and formulate the obtained equation as a linear system

$$(\mathsf{Q}^N - I)\mathbf{e} = \sum_{i=0}^{N-1} (\mathsf{Q}^i \mathscr{D}^{-1}\mathscr{F}^{(N-1)-i}), \tag{37}$$

where $\mathbf{e}$ is the initial condition minimizing the absolute value of $U^N - U^0$, thereby giving the solution of the corresponding time-harmonic problem. We then multiply Equation (37) on the left by $(\mathsf{Q}^N - I)^T\mathsf{M}$ to get a linear system

$$\mathsf{A}\mathbf{e} = \mathsf{b}, \tag{38}$$

where

$$\mathsf{A} = (\mathsf{Q}^N - I)^T\mathsf{M}(\mathsf{Q}^N - I), \tag{39}$$

$$\mathsf{b} = (\mathsf{Q}^N - I)^T\mathsf{M}\sum_{i=0}^{N-1} (\mathsf{Q}^i \mathscr{D}^{-1}\mathscr{F}^{(N-1)-i}). \tag{40}$$

In principle, if the coefficient matrix and the right-hand side vector in Equation (38) (respectively, in Equation (35)) are known explicitly, the linear system could be solved by a direct method, such as LU decomposition. However, we are considering three-dimensional problems for which it is challenging to find decompositions with a low number of non-zero elements. Also getting the matrix entries, requiring solving the time-dependent problem, is computationally expensive. Thus, iterative methods are preferred over the direct ones. For the sake of computational efficiency, we proceed to formulate an optimization problem that has its solution equal to the solution of Equation (38).

Remark 1. To obtain Equation (38), we essentially multiply Equation (37) by $(\mathsf{Q}^N - I)$ using the weighted inner product defined as

$$\langle A, B \rangle = A^T\mathsf{M}B, \tag{41}$$

where M is a symmetric (or Hermitian) and positive definite matrix. The norm, corresponding to the inner product, is defined as $\|A\| = \sqrt{A^T\mathsf{M}A}$. By this inner product, the total energy of the system (see Equation (20)) can be written as

$$\mathscr{E}(U) = \tfrac{1}{2}\langle U, U \rangle = \tfrac{1}{2}\|U\|^2, \tag{42}$$

and it is preserved by the wave operator.

4.3. *Minimization problem*

We equivalently reformulate the problem as a least-squares optimization problem,

$$\min J(\mathbf{e}), \tag{43}$$

where the cost function $J(\mathbf{e})$ is the energy of the error between the final state and initial state,

$$J(\mathbf{e}) = \mathscr{E}(U^N - \mathbf{e}) = \tfrac{1}{2}(U^N - \mathbf{e})^T\mathsf{M}(U^N - \mathbf{e}) = \tfrac{1}{2}\mathbf{e}^T\mathsf{A}\mathbf{e} - \mathsf{b}^T\mathbf{e} + \mathsf{c}, \tag{44}$$

where A and b are provided by Equations (39) and (40), and

$$\mathsf{c} = \frac{1}{2}\sum_{i=0}^{N-1} (\mathsf{Q}^i \mathscr{D}^{-1}\mathscr{F}^{(N-1)-i})^T\mathsf{M}\sum_{i=0}^{N-1} (\mathsf{Q}^i \mathscr{D}^{-1}\mathscr{F}^{(N-1)-i}). \tag{45}$$

The matrix A is symmetric and positive definite. Further, $J(\mathbf{e})$ is convex and has a minimum at the point where the first derivative, the gradient of $J(\mathbf{e})$, is zero. Since the minimum value of the functional $J(\mathbf{e})$ is obtained at $\mathbf{e}^* = \arg\min_{\mathbf{e} \in \mathbb{R}^{m+n}} J(\mathbf{e})$, such that $\nabla J(\mathbf{e}^*) = A\mathbf{e}^* - b = 0$, minimizing Equation (44) is equivalent to solving the linear system (38), and the minimum value of the functional is $J(\mathbf{e}^*) = \min_{\mathbf{e} \in \mathbb{R}^{m+n}} J(\mathbf{e}) = -b^T A^{-1} b / 2 + c$.

The Newton and quasi-Newton methods, steepest descent, and conjugate gradient method are iterative methods suitable for solving unconstrained optimization problems. Since we are looking forward to solving large problems, the feasible optimization algorithms are restricted to the methods with small memory requirements. Since the Hessian matrix of $J(\mathbf{e})$ is $\nabla^2 J(\mathbf{e}) = A$ and is not straightforwardly available, we neglect the Newton-type methods requiring the Hessian matrix or its approximation. Thus, we continue to consider how we can construct the gradient of the cost function with a computationally efficient procedure.

4.4. *Gradient*

The gradient of the cost function J is formulated by the adjoint equation technique as

$$\frac{dJ(\mathbf{e}, \mathbf{u}(\mathbf{e}))}{d\mathbf{e}} = \frac{\partial J(\mathbf{e}, \mathbf{u})}{\partial \mathbf{e}} - \mathbf{z}^T \frac{\partial S(\mathbf{e}, \mathbf{u})}{\partial \mathbf{e}}, \tag{46}$$

where the partial derivative of the cost function (44) with respect to the initial condition is

$$\frac{\partial J(\mathbf{e}, \mathbf{u})}{\partial \mathbf{e}} = M(\mathbf{e} - U^N), \tag{47}$$

and $\mathbf{z} = (z_0, z_1)^T$ is the solution of the adjoint state equation,

$$\left(\frac{\partial S(\mathbf{e}, \mathbf{u})}{\partial \mathbf{u}} \right)^T \mathbf{z} = \left(\frac{\partial J(\mathbf{e}, \mathbf{u})}{\partial \mathbf{u}} \right)^T. \tag{48}$$

Further, $\mathbf{z}$ includes the adjoint variables $\mathbf{z}^k = (z_0{}^k, z_1{}^k)^T = (z_0(t^k - (\Delta t/2)), z_1(t^k))^T$ for timesteps $k = 0, \ldots, N$. By Equation (44), we solve the right-hand side of Equation (48); that is,

$$\frac{\partial J(\mathbf{e}, \mathbf{u})}{\partial \mathbf{u}^k} = \begin{cases} M(U^N - \mathbf{e}), & \text{if } k = N, \\ 0, & \text{otherwise.} \end{cases} \tag{49}$$

Based on Equation (48), we now present the adjoint equation corresponding to the state equation (25) as a system

$$\begin{pmatrix} I & \mathscr{C}^T & & & & \\ & \mathscr{D}^T & \mathscr{C}^T & & & \\ & & \mathscr{D}^T & \mathscr{C}^T & & \\ & & & \ddots & \ddots & \\ & & & & \mathscr{D}^T & \mathscr{C}^T \\ & & & & & \mathscr{D}^T \end{pmatrix} \begin{pmatrix} Z^0 \\ Z^1 \\ \vdots \\ \vdots \\ Z^{N-1} \\ Z^N \end{pmatrix} = \begin{pmatrix} 0 \\ 0 \\ \vdots \\ \vdots \\ 0 \\ M(U^N - \mathbf{e}) \end{pmatrix}, \tag{50}$$

where Z^k is the vector of the adjoint state variables $z_0{}^k$ and $z_1{}^k$ for $k = N, \ldots, 0$. To solve Equation (50), we start with

$$Z^N = (\mathscr{D}^T)^{-1} M(U^N - \mathbf{e}), \tag{51}$$

continue by computing

$$Z^k = \begin{pmatrix} z_0{}^k \\ z_1{}^k \end{pmatrix} = -(\mathscr{D}^T)^{-1} \mathscr{C}^T Z^{k+1}, \tag{52}$$

at each time step $k = N - 1, \ldots, 1$, and finally get the solution

$$Z^0 = -\mathscr{C}^T Z^1. \tag{53}$$

To formulate the gradient of the cost function, we need, in addition to the solution of the adjoint state equation, the partial derivative of the state equation with respect to the initial condition. By Equation (25), we get $\partial S(\mathbf{e}, \mathbf{u})/\partial \mathbf{e} = (-I, 0, 0, \ldots, 0)^T$, implying $\mathbf{z}^T (\partial S(\mathbf{e}, \mathbf{u})/\partial \mathbf{e}) = -\mathbf{z}^0$. Consequently, by Equation (46), the gradient of the discretized cost function (44) is

$$\frac{\mathrm{d}J(\mathbf{e}, \mathbf{u}(\mathbf{e}))}{\mathrm{d}\mathbf{e}} = \mathsf{M}(\mathbf{e} - U^N) + Z^0. \tag{54}$$

4.5. *Conjugate gradient algorithm*

The conjugate gradient (CG) method, which provides a well-suited optimization algorithm for problems with quadratic objective functional and linear state equations, is a standard choice for the exact controllability approach. We use a starting point $\mathbf{e}^0$ and a A-conjugate set of vectors of successive directions $\{\mathbf{w}^0, \mathbf{w}^1, \ldots, \mathbf{w}^{\hat{N}-1}\}$. Since the vectors $\mathbf{w}^0, \mathbf{w}^1, \ldots, \mathbf{w}^{\hat{N}-1}$ form the basis, we can write the vector representing the move from $\mathbf{e}^0$ to the minimum point $\mathbf{e}^*$ as a linear combination of these vectors, such that,

$$\mathbf{e}^* = \mathbf{e}^0 + \sum_{i=0}^{\hat{N}-1} \eta^i \mathbf{w}^i = \mathbf{e}^k + \sum_{i=k}^{\hat{N}-1} \eta^i \mathbf{w}^i, \tag{55}$$

where η^i, $i = 0, \ldots, \hat{N} - 1$ are scalars. Multiplying Equation (55) by $(\mathbf{w}^j)^T \mathsf{A}$, substituting b for $\mathsf{A}\mathbf{e}^*$, and eliminating the cross terms based on A-conjugacy gives

$$\eta^i = \frac{-(\mathbf{w}^i)^T \mathbf{g}^i}{(\mathbf{w}^i)^T \mathsf{A}\mathbf{w}^i}, \tag{56}$$

where $\mathbf{g}^i = \mathsf{A}\mathbf{e}^i - \mathsf{b}$ is the gradient of J at point $\mathbf{e}^i$. Since $\mathbf{g}^i - \mathbf{g}^{i-1} = \mathsf{A}(\mathbf{e}^i - \mathbf{e}^{i-1})$, we compute the gradient by $\mathbf{g}^i = \mathbf{g}^{i-1} + \eta^{i-1} \mathsf{A}\mathbf{w}^{i-1}$. The first search direction is chosen to be the direction of the steepest descent $\mathbf{w}^0 = -\nabla J(\mathbf{e}^0)$. The new direction is determined as a linear combination of the steepest descent direction and the previous direction by using the scaling factor γ^i. Hence, we get the following algorithm:

Algorithm 1. *CG algorithm*

    Set the initial value $\mathbf{e}^0 = (\mathbf{e}_0^0, \mathbf{e}_1^0)^T$.

    Compute the gradient $\mathbf{g}^0 = \mathsf{A}\mathbf{e}^0 - \mathsf{b}$.

    Set $\mathbf{w}^0 = -\mathbf{g}^0$.

    Set $c_0 = -(\mathbf{w}^0, \mathbf{g}^0)$, $c_1 = c_0$, and $i = 1$.

    Repeat until $\sqrt{\frac{c_1}{c_0}} < \varepsilon$

        Compute the gradient update $\mathbf{v}^{i-1} = \mathsf{A}\mathbf{w}^{i-1}$.

        Compute $\eta^{i-1} = \frac{c_1}{(\mathbf{w}^{i-1}, \mathbf{v}^{i-1})}$.

        Update the control vector $\mathbf{e}^i = \mathbf{e}^{i-1} + \eta^{i-1} \mathbf{w}^{i-1}$.

        Update the residual vector $\mathbf{g}^i = \mathbf{g}^{i-1} + \eta^{i-1} \mathbf{v}^{i-1}$.
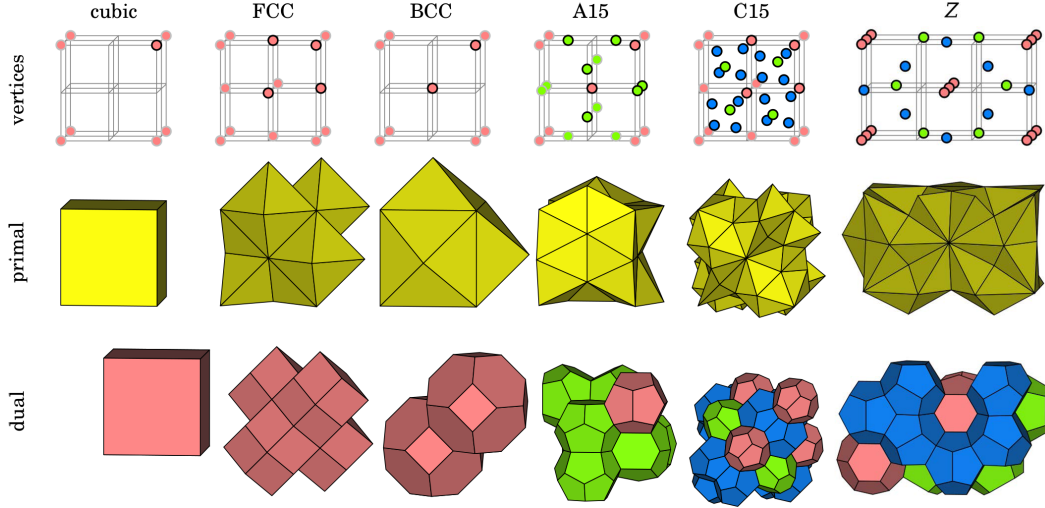
        Set $\mathbf{v}^i = -\mathbf{g}^i$.

        Compute $\gamma^{i-1} = \frac{1}{c_1}$, $c_1 = -(\mathbf{v}^i \mathbf{g}^i)$, and $\gamma^{i-1} = c_1 \gamma^{i-1}$.

        Update minimizing direction $\mathbf{w}^i = \mathbf{v}^i + \gamma^{i-1} \mathbf{w}^{i-1}$.

        Set $i = i + 1$,

where i refers to the number of iterations, ε is the stopping criterion, and $\sqrt{c_1/c_0}$ is the relative Euclidean norm of the residual. The values of the control variables $\mathbf{e}$ at the ith iteration are denoted by $\mathbf{e}_0^i$ and $\mathbf{e}_1^i$.

Figure 1. The vertex positions and primal and dual cells of the selected grid types [14, 15].

5. Numerical experiments

In this section, we demonstrate the accuracy of the method and show its performance for a non-convex domain. In both test cases, the interior of a three-dimensional obstacle is discretized by the six different grid types that we used earlier in transient wave simulations (see Figure 1 and references [14, 15, 27]). The grid types are cubic, face-centered cubic (FCC), body-centered cubic (BCC), A15, C15, and Z. The boundary of the obstacle is discretized by triangles and space between the boundary, and the interior grid is constructed by Voronoi tessellation. The boundary elements are also optimized by the HOT method [50] to improve element quality. Within each of the grid types, we have run the tests with several mesh resolutions. Both the conventional Yee's discrete Hodge operator and the one adapted to time-periodic problems are considered to show the advantage of the harmonic corrections. In [15], we showed that the energy is conserved in the time integration also at the discrete level. The residual of the controllability algorithm defines at each iteration how far the solution is from a periodic one. The CG iterations were continued until the relative norm of the residual was smaller than 10^{-5}. The simulations were run by an algorithm implemented in C++ programming language. The CPU times are considered as computed on Intel Xeon E5-2670 processors at 2.6 GHz.

5.1. *Convex obstacle*

We begin by demonstrating the performance of the method with a convex obstacle that is a sphere of radius 2.5. Inside the sphere we have set $\mu = 1$, $\sigma_E = 0.032$, $\sigma_H = 0$. The boundary surface is stretched in a radial direction, so that a 1.7 thick layer is generated outside the sphere forming an enlarged domain of radius 4.2. The 1.5 thick PML is initialized on the outermost part of the enlarged domain using the conductivities σ_E and σ_H for the outgoing wave by the relation

$$\frac{\sigma_E}{\epsilon} = \frac{\sigma_H}{\mu} = 0.5x, \tag{57}$$

where x is the distance from the inner interface of the layer.

The incident wave is a fully polarized plane wave with angular frequency $\omega = 2\pi$ propagating in the direction of the positive x_1-axis. The simulation solutions are observed at the inner
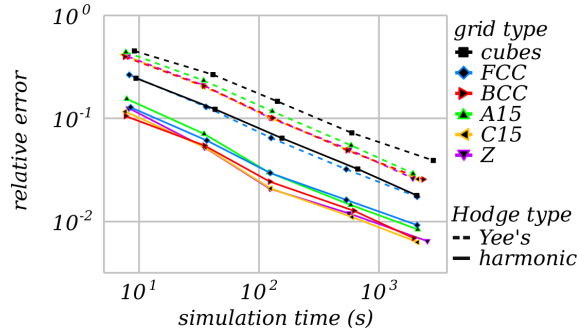
Figure 2. Relative error of the Mueller matrix, integrated over all scattering directions.

boundary of the PML at the radius 2.7. To report the accuracy of the method, the near-field so-lution is transferred to far-field scattering results by applying a near-field to far-field transforma-tion [51, 52]. The far-field scattering data are applied to produce the Mueller matrix [53] charac-terizing how a material interacts with electromagnetic waves and providing information about scattering intensities and polarization in all scattering directions. The accuracy is evaluated by comparing the Mueller matrix solution with the analytical Mie scattering solution [54]. Figure 2 illustrates the relative error of the Mueller matrices compared to the exact Mie solution for each grid type with five different mesh resolutions (numbers of elements per wavelength). We see that the harmonic correction improves the accuracy of the method with all the grid types. The most accurate results, obtained with the C15- and Z-grids and harmonic correction with respect to space and time, are almost an order of magnitude more accurate than the least accurate results obtained with the cubical grid and conventional Yee's discrete Hodge operator.

5.2. *Non-convex obstacle*

In the second test, we use the Stanford bunny [55] as a non-convex obstacle (see Figure 3). Inside the bunny, we set $\epsilon = 4$ and $\mu = 1$, while the media surrounding the bunny is modeled with $\epsilon = 1$ and $\mu = 1$. The bunny, with height 6.173 (from ear tip to the ground), length 5.265, and depth 4.782, is centered in a rectangular prism of height 9.453, length 9.508, and depth 8.107. The outermost layer, of thickness 1.5, of the rectangular prism features the PML condition of Equation (57). In the interior of the obstacle, we constructed for each grid type a set of grids with varying resolution. Outside the obstacle, we used a regular grid with an edge length of one tenth of the wavelength. As an incident wave, we used a circularly polarized plane wave propagating in the direction of the positive x_1-axis.

The simulation result is illustrated in Figure 3. The red, green, and blue components in the illustration present the x_1, x_2, and x_3 components of the electric field, respectively. There can be seen a little over five scattering waves in the horizontal direction inside the bunny, which is in good agreement with the wavelength and the bunny's width. To assess the accuracy, the reference solution is computed with the BCC grid with 40 elements per wavelength, and the results of the electric and magnetic wave components compared with the reference solution are shown in Figure 4. Again, we observe a significant difference between the errors computed with the conventional Yee's discrete Hodge operator and with the harmonic Hodge operator. When the harmonic Hodge operator is used, the cubical grid is the most inaccurate, but there are only slight differences in accuracy between the other grid types.

In the last examples, we used the BCC type bunny mesh with 50,190 nodes, 269,621 edges, and 403,215 faces to compare the control method with the asymptotic approach and to consider
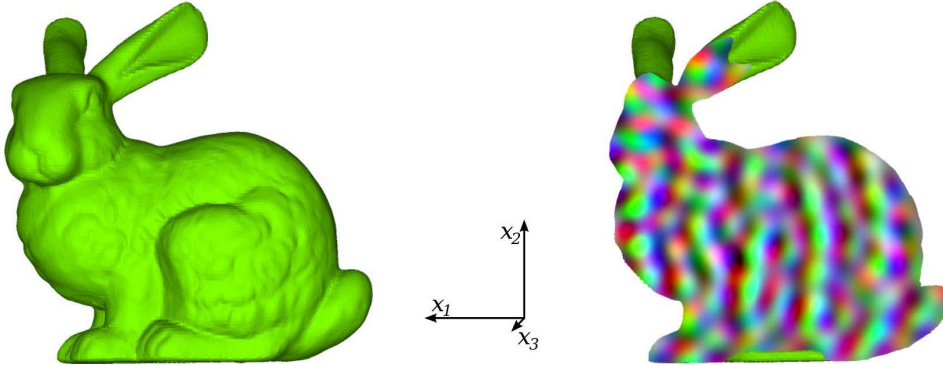
Figure 3. The Stanford bunny object is illustrated on the left-hand side. The x_1–x_3 plane cross-section of the interior scattered field is illustrated on the right-hand side.
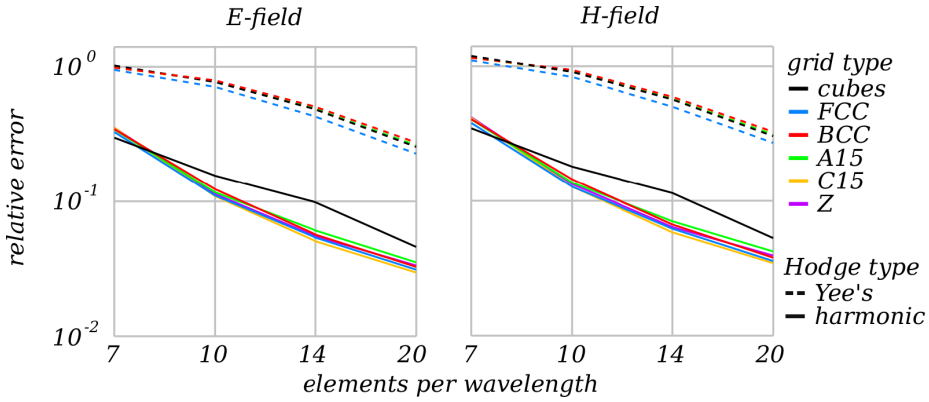

**Figure 4.** Relative error of the interior scattered fields.

the number of iterations required by the control method with increasing angular frequency. In these tests, we truncated the bunny by applying the Silver–Müller boundary condition without additional absorbing layers. We found that despite each iteration of the control method involves solving both the state and adjoint state equations, it remains more efficient than the asymptotic approach (see Figure 5). This is because the number of iterations required by the control method is less than half of the number of time periods needed for the asymptotic approach to achieve the accuracy level of the stopping criterion of the control method. Figure 6 shows the convergence of the control method at four different angular frequencies. The number of iterations increases with the angular frequency.

6. Conclusion

We presented a four-dimensional origin of the electromagnetic wave problem and derived from it a differential form formulation where the spatial and temporal variables are separated. We completed the discretization in space by the discrete exterior calculus. Since our main focus was on time-harmonic problems, to improve the accuracy, we applied an exact time-stepping scheme and a harmonic correction on the Hodge operator matrices used at the discrete level. In principle, we used a transient wave solver with space and time discretization adapted to time-periodic
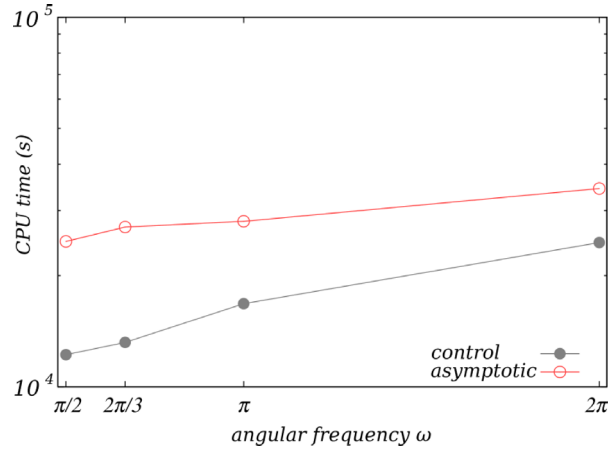
Figure 5. Comparison of CPU usage between the exact controllability method and the asymptotic approach at various angular frequencies.
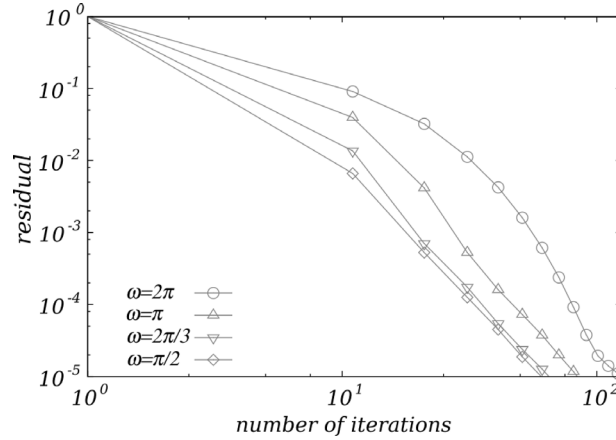
Figure 6. Number of iterations of the exact controllability method at various angular frequencies.

problems. We further accelerated the convergence to the time-harmonic solution by using the exact controllability approach realized by the conjugate gradient method. The energy norm is a weighted L^2-norm, and we minimize the discrete quadratic functional spanned by a diagonal mass matrix. Thus, the conjugate gradient algorithm operates in an L^2-type Hilbert space, and no preconditioning is needed. The numerical results demonstrate the accuracy improvements of the harmonic corrections. They also show the capability of the exact controllability method with the chosen discretization strategies in non-convex domains.

Declaration of interests

The authors do not work for, advise, own shares in, or receive funds from any organization that could benefit from this article, and have declared no affiliations other than their research organizations.

Dedication

The manuscript was written through contributions of all authors. All authors have given approval to the final version of the manuscript.

Acknowledgments

References

[1] S. C. Chen, W. C. Chew, "Electromagnetic theory with discrete exterior calculus", *Progr. Electromagn. Res.* **159** (2017), p. 59-78.

[2] L. da Silva, C. Batista, I. González, A. Macêdo, W. de Oliveira, S. Melo, "A discrete exterior calculus approach to quantum transport and quantum chaos on surface", *J. Comput. Theor. Nanosci.* **16** (2019), no. 9, p. 3670-3682.

[3] P. D. Boom, O. Kosmas, L. Margetts, A. P. Jivkov, "A geometric formulation of linear elasticity based on discrete exterior calculus", *Int. J. Solids Struct.* **236** (2022), article no. 111345.

[4] J. B. Perot, C. J. Zusi, "Differential forms for scientists and engineers", *J. Comput. Phys.* **257, Part B** (2014), p. 1373-1393.

[5] D. N. Arnold, P. B. Bochev, R. B. Lehoucq, R. A. Nicolaides, M. Shashkov (eds.), *Compatible Spatial Discretizations*, The IMA Volumes in Mathematics and its Applications, vol. 142, Springer, New York, USA, 2006.

[6] S. H. Christiansen, H. Z. Munthe-Kaas, B. Owren, "Topics in structure-preserving discretization", *Acta Numer.* **20** (2011), p. 1-119.

[7] H. Cartan, *Differential Forms*, Kershaw Publishing Company, London, 1971.

[8] M. Desbrun, A. N. Hirani, M. Leok, J. E. Marsden, "Discrete exterior calculus", 2005, preprint, https://arxiv.org/abs/math/0508341v2.

[9] A. Bossavit, L. Kettunen, "Yee-like schemes on a tetrahedral mesh, with diagonal lumping", *Int. J. Numer. Model.* **12** (1999), no. 1–2, p. 129-142.

[10] M. Desbrun, E. Kanso, Y. Tong, "Discrete differential forms for computational modeling", *Discrete Differ. Geom. Oberwolfach Semin.* **38** (2008), p. 287-324.

[11] S. H. Christiansen, F. Rapetti, "On high order finite element spaces of differential forms", *Math. Comput.* **85** (2016), no. 298, p. 517-548.

[12] R. Picard, S. Trostorff, M. Waurick, "Well-posedness via monotonicity—an overview", in *Operator Semigroups Meet Complex Analysis, Harmonic Analysis and Mathematical Physics*, Springer, Cham, Switzerland, 2015, p. 397-452.

[13] R. Picard, S. Trostorff, M. Waurick, "On a connection between the Maxwell system, the extended Maxwell system, the Dirac operator and gravito-electromagnetism", *Math. Methods Appl. Sci.* **40** (2017), no. 2, p. 415-434.

[14] J. Räbinä, S. Mönkölä, T. Rossi, "Efficient time integration of Maxwell's equations by generalized finite-differences", *SIAM J. Sci. Comput.* **37** (2015), no. 6, p. B834-B854.

[15] J. Räbinä, L. Kettunen, S. Mönkölä, T. Rossi, "Generalized wave propagation problems and discrete exterior calculus", *ESAIM: Math. Model. Numer. Anal.* **52** (2018), no. 3, p. 1195-1218.

[16] M. O. Bristeau, R. Glowinski, J. Périaux, "Controllability methods for the computation of time-periodic solutions; application to scattering", *J. Comput. Phys.* **147** (1998), no. 2, p. 265-292.

[17] R. Glowinski, "Ensuring well-posedness by analogy; Stokes problem and boundary control for the wave equation", *J. Comput. Phys.* **103** (1992), no. 2, p. 189-221.

[18] M. O. Bristeau, R. Glowinski, J. Périaux, "Numerical simulation of high frequency scattering waves using exact controllability methods", in *Nonlinear Hyperbolic Problems: Theoretical, Applied, and Computational Aspects: Proceedings of the Fourth International Conference on Hyperbolic Problems, Taormina, Italy, April 3–8, 1992*, Vieweg+Teubner Verlag, Wiesbaden, Germany, 1993, p. 86-108.

[19] M. O. Bristeau, R. Glowinski, J. Périaux, "Scattering waves using exact controllability methods", in *31st Aerospace Sciences Meeting*, American Institute of Aeronautics and Astronautics, Washington, USA, 1993.

[20] M. O. Bristeau, R. Glowinski, J. Périaux, T. Rossi, "3D harmonic Maxwell solutions on vector and parallel computers using controllability and finite element methods", Tech. Report RR-3607, INRIA, 1999.

[21] R. Glowinski, T. Rossi, "A mixed formulation and exact controllability approach for the computation of the periodic solutions of the scalar wave equation. (I) Controllability problem formulation and related iterative solution", *C. R. Acad. Sci. Paris* **343** (2006), no. 7, p. 493-498.

[22] S. Kähkönen, R. Glowinski, T. Rossi, R. Mäkinen, "Solution of time-periodic wave equation using mixed finite-elements and controllability techniques", *J. Comput. Acoust.* **19** (2011), no. 4, p. 335-352.

[23] T. Chaumont-Frelet, M. J. Grote, S. Lanteri, J. H. Tang, "A controllability method for Maxwell's equations", *SIAM J. Sci. Comput.* **44** (2022), no. 6, p. A3700-A3727.

[24] J. Räbinä, "On a numerical solution of the Maxwell equations by discrete exterior calculus", Phd thesis, University of Jyväskylä, 2014, http://urn.fi/URN:ISBN:978-951-39-5951-7.

[25] D. Pauly, T. Rossi, "Theoretical considerations on the computation of generalized time-periodic waves", *Adv. Math. Sci. Appl.* **21** (2011), no. 1, p. 105-131.

[26] J. Räbinä, P. Kuopanportti, M. Kivioja, M. Möttönen, T. Rossi, "Three-dimensional splitting dynamics of giant vortices in Bose–Einstein condensates", *Phys. Rev. A* **98** (2018), article no. 023624.

[27] M. Kivioja, S. Mönkölä, T. Rossi, "GPU-accelerated time integration of Gross–Pitaevskii equation with discrete exterior calculus", *Comput. Phys. Commun.* **278** (2022), article no. 108427.

[28] M. Kivioja, R. Zamora-Zamora, A. Blinova, S. Mönkölä, T. Rossi, M. Möttönen, "Evolution and decay of an Alice ring in a spinor Bose–Einstein condensate", *Phys. Rev. Res.* **5** (2023), no. 2, article no. 023104.

[29] T. Rossi, J. Räbinä, S. Mönkölä, S. Kiiskinen, J. Lohi, L. Kettunen, "Systematisation of systems solving physics boundary value problems", in *Numerical Mathematics and Advanced Applications ENUMATH 2019: European Conference, Egmond aan Zee, The Netherlands, September 30–October 4*, Springer, Cham, Switzerland, 2020, p. 35-51.

[30] L. Kettunen, T. Rossi, "Systematic derivation of partial differential equations for second order boundary value problems", *Int. J. Numer. Model.: Electronic Networks, Devices and Fields* **36** (2023), no. 3, article no. e3078.

[31] J. Lohi, L. Kettunen, "Whitney forms and their extensions", *J. Comput. Appl. Math.* **393** (2021), article no. 113520.

[32] L. Kettunen, J. Lohi, J. Räbinä, S. Mönkölä, T. Rossi, "Generalized finite difference schemes with higher order Whitney forms", *ESAIM: Math. Model. Numer. Anal.* **55** (2021), no. 4, p. 1439-1460.

[33] J. Lohi, "Systematic implementation of higher order Whitney forms in methods based on discrete exterior calculus", *Numer. Algorithms* **91** (2022), no. 3, p. 1261-1285.

[34] E. Heikkola, S. Mönkölä, A. Pennanen, T. Rossi, "Controllability method for the Helmholtz equation with higher-order discretizations", *J. Comput. Phys.* **225** (2007), no. 2, p. 1553-1576.

[35] S. Mönkölä, E. Heikkola, A. Pennanen, T. Rossi, "Time-harmonic elasticity with controllability and higher order discretization methods", *J. Comput. Phys.* **227** (2008), no. 11, p. 5513-5534.

[36] S. Mönkölä, "An optimization-based approach for solving a time-harmonic multiphysical wave problem with higher-order schemes", *J. Comput. Phys.* **242** (2013), p. 439-459.

[37] J. H. Tang, R. Brossier, L. Métivier, "Fully scalable solver for frequency-domain visco-elastic wave equations in 3D heterogeneous media: a controllability approach", *J. Comput. Phys.* **468** (2022), article no. 111514.

[38] A. Lew, J. E. Marsden, M. Ortiz, M. West, "Asynchronous variational integrators", *Arch. Rational Mech. Anal.* **167** (2003), no. 2, p. 85-146.

[39] A. Stern, Y. Tong, M. Desbrun, J. E. Marsden, "Geometric computational electrodynamics with variational integrators and discrete differential forms", in *Geometry, Mechanics, and Dynamics: The Legacy of Jerry Marsden*, Springer, New York, USA, 2015, p. 437-475.

[40] C. Ma, Z. Chen, "Stability and numerical dispersion analysis of CE-FDTD method", *IEEE Trans. Antennas Propag.* **53** (2005), no. 1, p. 332-338.

[41] Z. Peng, D. Appelö, "EM-WaveHoltz: a flexible frequency-domain method built from time-domain solvers", *IEEE Trans. Antennas Propag.* **70** (2022), no. 7, p. 5659-5671.

[42] I. Lindell, *Differential Forms in Electromagnetics*, IEEE Press Series on Electromagnetic Wave Theory, Wiley, New Jersey, USA, 2004.

[43] K. F. Warnick, P. H. Russer, "Differential forms and electromagnetic field theory", *Progr. Electromagnet. Res.* **148** (2014), p. 83-112.

[44] C. von Westenholz, *Differential Forms in Mathematical Physics*, Studies in Mathematics and its Applications, North Holland, Amsterdam, Netherlands, 1978.

[45] A. N. Hirani, K. Kalyanaraman, E. B. VanderZee, "Delaunay Hodge star", *Comput. Aided Des.* **45** (2013), no. 2, p. 540-544, Solid and Physical Modeling 2012.

[46] S. Mönkölä, J. Räty, "Discrete exterior calculus for photonic crystal waveguides", *Int. J. Numer. Methods Eng.* **124** (2023), no. 5, p. 1035-1054.

[47] B. Hanouzet, M. Sesques, "Absorbing boundary conditions for Maxwell's equations", in *Nonlinear Hyperbolic Problems: Theoretical, Applied, and Computational Aspects*, Vieweg+Teubner Verlag, Wiesbaden, Germany, 1993, p. 315-322.

[48] J.-P. Berenger, "A perfectly matched layer for the absorption of electromagnetic waves", *J. Comput. Phys.* **114** (1994), no. 2, p. 185-200.

[49] J. Räbinä, S. Mönkölä, T. Rossi, A. Penttilä, K. Muinonen, "Comparison of discrete exterior calculus and discrete-dipole approximation for electromagnetic scattering", *J. Quant. Spectrosc. Rad. Transf.* **146** (2014), p. 417-423.

[50] P. Mullen, P. Memari, F. de Goes, M. Desbrun, "HOT: Hodge-optimized triangulations", *ACM Trans. Graph.* **30** (2011), no. 4, article no. 103, p. 1–12.

[51] K. Umashankar, A. Taflove, "A novel method to analyse electromagnetic scattering of complex object", *IEEE Trans. Electromagn. Compat.* **24** (1982), no. 4, p. 397-405.

[52] A. Taflove, K. Umashankar, "Radar cross section of general three-dimensional scatterers", *IEEE Trans. Electromagn. Compat.* **25** (1983), no. 4, p. 433-440.

[53] C. F. Bohren, D. R. Huffman, *Absorption and Scattering of Light by Small Particles*, Wiley & Sons, New York, 1983, 53-56 pages.

[54] C. Mätzler, "MATLAB Functions for Mie scattering and absorption. Version 2", Tech. Report 2002–11, Institute of Applied Physics, University of Bern, 2002.

[55] G. Turk, M. Levoy, "Zippered polygon meshes from range images", in *Proceedings of the 21st Annual Conference on Computer Graphics and Interactive Techniques, SIGGRAPH '94*, ACM, New York, NY, USA, 1994, p. 311-318.